High-temperature superconductivity in the Ti-H system at high pressures

Jin Zhang,[1] Jeffrey M. McMahon,[1,*] Artem R. Oganov,[2,3,4,†] Xinfeng Li,[5] Xiao Dong,[6] Huafeng Dong,[7] and Shengnan Wang[8]

[1]*Department of Physics and Astronomy, Washington State University, Pullman, Washington 99164, USA*
[2]*Skolkovo Institute of Science and Technology, Skolkovo Innovation Center, 3 Nobel St., Moscow 143026, Russia*
[3]*Moscow Institute of Physics and Technology, 9 Institutskiy Lane, Dolgoprudny 141700, Russia*
[4]*International Center for Materials Discovery, Northwestern Polytechnical University, Xi'an, Shaanxi 710072, China*
[5]*Sino-French Institute of Nuclear Engineering and Technology, Sun Yat-sen University, Zhuhai, Guangzhou 519082, China*
[6]*Key Laboratory of Weak-Light Nonlinear Photonics and School of Physics, Nankai University, Tianjin 300071, China*
[7]*School of Physics and Optoelectronic Engineering, Guangdong University of Technology, Guangzhou 510006, China*
[8]*Department of Geosciences, Center for Materials by Design, and Institute for Advanced Computational Science, State University of New York, Stony Brook, New York 11794-2100, USA*

(Received 20 November 2019; revised manuscript received 13 February 2020; accepted 9 March 2020; published 17 April 2020)

Search for stable high-pressure compounds in the Ti-H system reveals the existence of titanium hydrides with new stoichiometries, including $Ibam$-Ti_2H_5, $I4/m$-Ti_5H_{13}, $I\bar{4}$-Ti_5H_{14}, $Fddd$-TiH_4, $Immm$-Ti_2H_{13}, $P\bar{1}$-TiH_{12}, and $C2/m$-TiH_{22}. Our calculations predict $I4/mmm \rightarrow R\bar{3}m$ and $I4/mmm \rightarrow Cmma$ transitions in TiH and TiH_2, respectively. Phonons and the electron-phonon coupling in all searched titanium hydrides are analyzed at high pressure. It is found that $Immm$-Ti_2H_{13}, rather than the hydrogen-richest $C2/m$-TiH_{22}, exhibits the highest superconducting critical temperature T_c. The estimated T_c of $Immm$-Ti_2H_{13} and $C2/m$-TiH_{22} are, respectively, 127.4–149.4 K ($\mu^* = 0.1$–0.15) at 350 GPa and 91.3–110.2 K at 250 GPa, as found by numerically solving the Eliashberg equations.

DOI: 10.1103/PhysRevB.101.134108

I. INTRODUCTION

Enthusiasm for discovering high-temperature superconductors never ceased [1] since solid mercury was discovered to have zero electrical resistance below 4.2 K in 1911 [2]. In recent years, especially at high pressure, the record of the critical temperature (T_c) of superconductivity has been quickly and repeatedly broken in both experimental and theoretical studies, rendering the ultimate goal for synthesizing a room-temperature superconductor (T_c at around 298 K) to be apparently within reach. In 2014, first-principles calculation [3] based on density functional theory (DFT) predicted the T_c of $Im\bar{3}m$-H_3S to be in the range 191 K–204 K at 200 GPa. Subsequently, the diamond anvil cell (DAC) experiment in 2015 [4] verified this prediction and reported the T_c of sulfur hydride of 203 K at 150 GPa. In 2017, DFT calculation [5] estimated T_c of $Fm\bar{3}m$-LaH_{10} to be 274–286 K at 210 GPa and of $Fm\bar{3}m$-YH_{10} to be 305–326 K (the highest theoretically calculated T_c for simple binary systems so far [6]) at 250 GPa. Soon afterward, the teams of Hemley [7] and Eremets [8] observed lanthanum hydride ($Fm\bar{3}m$-LaH_{10}) to be superconducting under pressure (170–200 GPa) with T_c of around 250–260 K, which is the highest T_c that has been experimentally confirmed. Although the effect of pressure on superconductivity is not fully understood [9,10], these new record high-T_c superconductors are conventional, phonon-mediated ones. Based on Bardeen-Cooper-Schrieffer (BCS) or Migdal-Eliashberg theories, pressure affects the T_c of conventional superconductors by modifying their electronic and phonon parameters, e.g., electronic density of states at the Fermi level, average phonon frequency, and electron-phonon coupling (EPC) constant.

Motivation for investigating superconductivity of hydrides under pressure originally came from both the possibility that metallic hydrogen under high pressure could be a high-temperature superconductor [11] and from the viewpoint that the pressure of metallization of hydrogen-rich solids can be considerably lower than that of pure hydrogen [12,13]. Since carrying out the high-pressure experiments is expensive and technically challenging, many of the investigations on these superconductors are performed computationally using crystal structure prediction techniques. Aside from $Im\bar{3}m$-H_3S, $Fm\bar{3}m$-LaH_{10}, and $Fm\bar{3}m$-YH_{10} (mentioned above), the calculated T_c of some predicted structures are as follows: $R\bar{3}m$-LiH_6 is 82 K at 300 GPa [14], $Im\bar{3}m$-MgH_6 is 271 K at 400 GPa [15], $Im\bar{3}m$-CaH_6 is 220–235 K at 150 GPa [16], $I4_1md$-ScH_9 is 233 K at 300 GPa [17], $Cmcm$-ZrH is 11 K at 120 GPa [18], $P2_1/m$-HfH_2 is 11–13 K at 260 GPa [19], $Fdd2$-TaH_6 is 124–136 K at 300 GPa [20], $Pm\bar{3}n$-GeH_3 is 140 K at 180 GPa [21], $P6/mmm$-LaH_{16} is 156 K at 200 GPa [22], $C2/m$-SnH_{14} is 86–97 K at 300 GPa [23], $Im\bar{3}m$-H_3Se is 131 at 200 GPa [24], $P6/mmm$-H_4Te is 95–104 at 170 GPa [25]. Almost all binary hydride systems have been computationally studied by now, at least crudely (see an overview in Ref. [26]).

*jeffrey.mcmahon@wsu.edu
†a.oganov@skoltech.ru

Transition metal hydrides can have a variety of stable stoichiometries and lower metallization pressure compared with other hydrides. Especially, those with high hydrogen content often contain unexpected hydrogen groups and exhibit intriguing properties. Based on recent ideas [26], Ti as an early $3d$-metal promises to form high-T_c superconducting hydrides. At ambient conditions, TiH_2 crystallizes in a tetragonal structure ($I4/mmm$), which transforms into a cubic phase ($Fm\bar{3}m$) at temperature increasing to 310 K [27,28]. DAC experiments [29–31] indicated that $I4/mmm$-TiH_2 remains stable at pressures up to 90 GPa at room temperature. The theoretically estimated T_c is 6.7 K ($\lambda = 0.84$, $\mu^* = 0.1$) for $Fm\bar{3}m$-TiH_2 and 2 mK ($\lambda = 0.22$, $\mu^* = 0.1$) for $I4/mmm$-TiH_2 [32] at ambient pressure.

In this paper, the crystal structures and superconductivity of titanium hydrides at pressures up to 350 GPa are systematically studied. In addition to $I4/mmm$-TiH_2, several new stoichiometries and phases are found at high pressure by the first principles evolutionary algorithm USPEX [33–35]. The predicted TiH_{22} becomes thermodynamically stable at pressure above 235 GPa and in its crystal structure Ti atoms are encapsulated in H_{20} cages. The dynamical stability of all high-pressure phases was verified by calculations of phonons throughout the Brillouin zone. Three different approaches are utilized to determine the superconducting T_c. The predicted T_c (obtained by numerically solving the Eliashberg equations) for $C2/m$-TiH_{22} and $Immm$-Ti_2H_{13} are 91.3–110.2 K (at 250 GPa) and 127.4–149.4 K (at 350 GPa), respectively. Our work provides clear guidance for future experimental investigation of potential high-temperature superconductivity in titanium hydrides under pressure.

II. COMPUTATIONAL METHODOLOGY

Variable-composition prediction of stable compounds in the Ti-H system was performed at 0, 50, 100, 150, 200, 250, 300, and 350 GPa with up to 24 atoms in the primitive cell through first-principles evolutionary algorithm (EA), as implemented in the USPEX code [33–35]. In addition, fixed-composition structure searches were performed for TiH_{24}, TiH_{26}, and TiH_{28} at 350 GPa. Structure relaxations were based on DFT within the Perdew-Burke-Ernzerhof (PBE) generalized gradient approximation (GGA) exchange-correlation functional [36], as implemented in the VASP package [37]. The electron-ion interaction was described by projector-augmented wave (PAW) potentials [39,40], with $3p^6 4s^2 3d^4$ and $1s^2$ shells treated as valence for Ti and H, respectively. The Brillouin zone (BZ) was sampled using Γ-centered uniform k meshes (with resolution $2\pi \times 0.05$ Å^{-1}) and the kinetic energy cutoff for the plane-wave basis set was 600 eV. For each crystal structure search, the maximum number of generations was set to 80. The initial generation consisting of 120 structures was created using random symmetric generator [35]. Each subsequent generation contained 100 structures produced from the previous generation using heredity (40%), lattice mutation (20%), and transmutation (20%) operators, and in addition, 20% of the structures were produced by random symmetric generator (20%).The compositional distribution searched at different pressures is illustrated in Fig. S1 in the Supplemental Material [38]. Structures predicted to be stable or low-enthalpy metastable were then carefully reoptimized to construct convex hull at each pressure, and then the pressure-composition phase diagram.

Phonon calculations were carried out using the finite-displacement method as implemented in the PHONOPY [41] code, using VASP to calculate the force constants matrix, and we performed separate calculations using density-functional perturbation theory (DFPT) [42] in the QUANTUM ESPRESSO (QE) package [43,44]. Results of these two methods were in perfect agreement. The EPC coefficients were calculated using DFPT in QE, the norm-conserving pseudopotentials (tested by comparing the phonon spectra with the results calculated using PHONOPY code) and the PBE functional. Convergence tests show that 120 Ry is a suitable cutoff energy for the plane-wave basis set in the QE calculation. A $4 \times 4 \times 4$ q mesh was used in the phonon and electron-phonon calculations.

T_c was estimated using three approaches: by numerically solving Eliashberg equations, and using modified McMillan and Allen-Dynes formulas. Starting from BCS theory, several first-principles Green's function methods had been proposed to calculate the superconducting properties. Migdal-Eliashberg formalism is one of these, and can accurately describe conventional superconductors [45]. Within the Migdal approximation [46], the adiabatic ratio $\lambda\omega_D/\epsilon_F$ ($\simeq \sqrt{m^*/M}$) is small since the vertex correction $O(\sqrt{m^*/M})$ can compare to the bare vertex and then be neglected. In the adiabatic ratio, m^* is the electron effective mass, M is the ion mass, ω_D is Debye frequency, and ϵ_F is Fermi energy. Then, T_c can be calculated by solving two nonlinear Eliashberg equations [47] (or isotropic gap equations) for the Matsubara gap (or superconducting order parameter) $\Delta_n \equiv \Delta(i\omega_n)$ and electron mass renormalization function (or wave-function renormalization factor) $Z_n \equiv Z(i\omega_n)$ along the imaginary frequency axis ($i = \sqrt{-1}$),

$$\Delta_n Z_n = \frac{\pi}{\beta} \sum_{m=-M}^{M} \frac{\lambda(\omega_n - \omega_m) - \mu^* \theta(\omega_c - |\omega_m|)}{\sqrt{\omega_m^2 + \Delta_m^2}} \Delta_m \quad (1)$$

and

$$Z_n = 1 + \frac{\pi}{\beta\omega_n} \sum_{m=-M}^{M} \frac{\lambda(\omega_n - \omega_m)}{\sqrt{\omega_m^2 + \Delta_m^2}} \omega_m, \quad (2)$$

where $\beta = 1/k_B T$, k_B is the Boltzmann constant, μ^* denotes the Coulomb pseudopotential, θ is the Heaviside function, ω_c is the phonon cutoff frequency: $\omega_c = 3\omega_{\max}$, $\omega_{\max}$ is the maximum phonon frequency, $\omega_n = (\pi/\beta)(2n) - 1)$ is the nth fermion Matsubara frequency with $n = 0, \pm 1, \pm 2, ...$, the pairing kernel for electron-phonon interaction (or, the electron-boson attraction between two electrons interacting around the Fermi energy [47]) possesses the form $\lambda(\omega_n - \omega_m) = 2\int_0^{\omega_{\max}} \frac{\alpha^2 F(\omega)\omega}{\omega^2 + (\omega_n - \omega_m)^2} d\omega$ and $\alpha^2 F(\omega)$ represents the Eliashberg spectral function. These two equations are derived with the help of thermodynamic Green's functions and the derivation was given in detail by Allen and Mitrović [48].

The important feature of the gap equations is that all the involved quantities only depend on the normal state, and then can be calculated from first principles. At each temperature T, the coupled equations need to be solved iteratively until

self-consistency. T_c is defined as the temperature at which the Matsubara gap Δ_n becomes zero. The Eliashberg equations have been solved numerically for 2201 Matsubara frequencies ($M = 1100$) in this paper. A detailed discussion of this numerical method was presented in Refs. [49,50].

In addition to the above numerical method, T_c can also be obtained by other two analytical formulas, which are widely used for their attractive simplicity and success in the case of small λ. The first one was developed by McMillan [51] and later refined by Allen and Dynes [52,53]. This formula is named as Allen-Dynes modified McMillan equation (using $\frac{\omega_{\log}}{1.2}$ in place of the prefactor $\frac{\Theta_D}{1.45}$ in McMillan equation) and is given as

$$T_c = \frac{\omega_{\log}}{1.20}\exp\left(-\frac{1.04(1+\lambda)}{\lambda-\mu^*(1+0.62\lambda)}\right), \tag{3}$$

where the logarithmic average frequency is defined as $\omega_{\log} = \exp(\frac{2}{\lambda}\int_0^{\omega_{\max}}\frac{\alpha^2F(\omega)}{\omega}\ln(\omega)d\omega)$, the isotropic EPC constant, which is a dimensionless measure of the average strength of the EPC, can be defined as $\lambda = 2\int_0^{\omega_{\max}}\frac{\alpha^2F(\omega)}{\omega}d\omega$.

The second analytical formula is established on the basis of Allen-Dynes modified McMillan equation [Eq. (3)], but with correction factors. These are added to increase the range of validity to higher values λ and to consider the influence of the shape of spectral density. The resulting expression is known as Allen-Dynes formula and is written as [53]

$$T_c = f_1 f_2\frac{\omega_{\log}}{1.20}\exp\left(-\frac{1.04(1+\lambda)}{\lambda-\mu^*(1+0.62\lambda)}\right), \tag{4}$$

where f_1 and f_2 are strong coupling correction and shape correction, respectively. These two factors are

$$f_1 = \left\{1+\left[\frac{\lambda}{2.46(1+3.8\mu^*)}\right]^{\frac{3}{2}}\right\}^{\frac{1}{3}} \tag{5}$$

and

$$f_2 = 1+\frac{\left(\frac{\bar{\omega}_2}{\omega_{\log}}-1\right)\lambda^2}{\lambda^2+3.312(1+6.3\mu^*)^2\left(\frac{\bar{\omega}_2}{\omega_{\log}}\right)^2}, \tag{6}$$

where $\bar{\omega}_2$ is defined as $\bar{\omega}_2 = [\frac{2}{\lambda}\int_0^{\omega_{\max}}\alpha^2F(\omega)\omega\, d\omega]^{\frac{1}{2}}$.

Regardless of which of the above three methods is used to calculate T_c, two main input quantities are needed. One is the Coulomb pseudopotential μ^*, which models the depairing interaction between the electrons. However, μ^* is hard to calculate from first principles. Here, we used standard values $\mu^* = 0.1$ and 0.15. The other one is the Eliashberg spectral function $\alpha^2F(\omega)$, which models the coupling of phonons to electrons on the Fermi surface. $\alpha^2F(\omega)$ can be calculated as [54]

$$\alpha^2F(\omega) = \frac{1}{2\pi N(\epsilon_F)}\sum_{\mathbf{q}\nu}\delta(\omega-\omega_{\mathbf{q}\nu})\frac{\gamma_{\mathbf{q}\nu}}{\omega_{\mathbf{q}\nu}}, \tag{7}$$

where $N(\epsilon_F)$ is the density of states at the Fermi level per unit cell per spin, $\mathbf{q}$ is the wave vector, $\omega_{\mathbf{q}}$ is the $\mathbf{q}$-point weight, $\omega_{\mathbf{q}\nu}$ is the screened phonon frequency, and $\gamma_{\mathbf{q}\nu}$ is the phonon linewidth, which is determined exclusively by the electron-phonon matrix elements $g^{\nu}_{mn}(\mathbf{k},\mathbf{q})$ with states on the Fermi surface, is given as

$$\gamma_{\mathbf{q}\nu} = \pi\omega_{\mathbf{q}\nu}\sum_{mn}\sum_{\mathbf{k}}\omega_{\mathbf{k}}\left|g^{\nu}_{mn}(\mathbf{k},\mathbf{q})\right|^2\delta(\epsilon_{m,\mathbf{k}+\mathbf{q}}-\epsilon_F) \times\delta(\epsilon_{n,\mathbf{k}}-\epsilon_F), \tag{8}$$

where $\omega_{\mathbf{k}}$ is the $\mathbf{k}$-point weight normalized to 2 in order to account for the spin degeneracy in spin-unpolarized calculations. $g^{\nu}_{mn}(\mathbf{k},\mathbf{q})$ is described as

$$g^{\nu}_{mn}(\mathbf{k},\mathbf{q}) = \left(\frac{\hbar}{2M\omega_{\mathbf{q}\nu}}\right)^{1/2}\langle m,\mathbf{k}+\mathbf{q}|\delta_{\mathbf{q}\nu}V_{\mathrm{SCF}}|n,\mathbf{k}\rangle, \tag{9}$$

where $|n,k\rangle$ is the bare electronic Bloch state, M is the ionic mass, and $\delta_{\mathbf{q}\nu}V_{\mathrm{SCF}}$ is the derivative of the self-consistent potential with respect to the collective ionic displacement corresponding to the phonon wave vector $\mathbf{q}$ and mode ν. In this work, $g^{\nu}_{mn}(\mathbf{k},\mathbf{q})$ is calculated within the harmonic approximation, using the QE package. Note that anharmonicity, which usually decreases T_c, is not included in our calculations.

III. RESULTS AND DISCUSSIONS

Thermodynamic convex hulls for the Ti-H system at several pressures are shown in Fig. 1. In our structure searches, experimentally reported $I4/mmm$-TiH_2 is found to be the only stable hydride at zero pressure. Lattice parameters were optimized to be $a = 3.208$ Å and $c = 4.203$ Å at 0 GPa, which is in good accordance with the experimental data ($a = 3.163$ Å and $c = 4.391$ Å) [29]. The calculated Gibbs free energy of formation of $I4/mmm$-TiH_2 is -0.3123 eV/atom at zero pressure and 298 K [red convex hull in Fig. 1(a)], which is in good agreement with the experimental value of -0.363 eV/atom [55] [blue dashed convex hull in Fig. 1(a)]. Aside from $I4/mmm$-TiH and $Fm\bar{3}m$-TiH_3, which were already predicted by Zhuang [56] under high pressure, several other phases and stoichiometries, including $R\bar{3}m$-TiH, $Cmma$-TiH_2, $Ibam$-Ti_2H_5, $I4/m$-Ti_5H_{13}, $I\bar{4}$-Ti_5H_{14}, $Fddd$-TiH_4, $Immm$-Ti_2H_{13}, $P\bar{1}$-TiH_{12}, $C2/m$-TiH_{14}, and $C2/m$-TiH_{22}, are predicted at pressures up to 350 GPa. No subhydrides (Ti_xH_y, $x > y$) show up in the Ti-H system at any pressure. The enthalpies of formation with and without including zero-point energy (ZPE) are depicted by red lines with open squares and black lines with solid squares in Figs. 1(b)–1(h), respectively. Taking ZPE into account did not significantly change the basic shape of convex hulls, but did make some changes at pressures above 250 GPa: considering ZPE made $I\bar{4}$-Ti_5H_{14} and $P\bar{1}$-TiH_{12} metastable [indicated in gray in Figs. 1(f)–1(h)] instead of stable structures above 250 GPa.

The pressure-composition phase diagram of Ti-H system is depicted in Fig. 2. Based on our calculations, the phase transition sequence of Ti under high pressure is $P6/mmm(\omega) \xrightarrow{104\ \mathrm{GPa}} Cmcm(\gamma) \xrightarrow{109\ \mathrm{GPa}} Cmcm(\delta) \xrightarrow{127\ \mathrm{GPa}} Im\bar{3}m(\beta)$. Although both γ-Ti and δ-Ti have the same space group and contain four titanium atoms in their unit cell, the structure of γ-Ti is a distortion of ω-Ti (hcp), while δ-Ti is more similar to β-Ti (bcc). Under high pressure, $P6_3/m$-H transforms into $C2/c$-H at 110 GPa and further into $Cmca$-H at 280 GPa. The crystal structures of these high-pressure

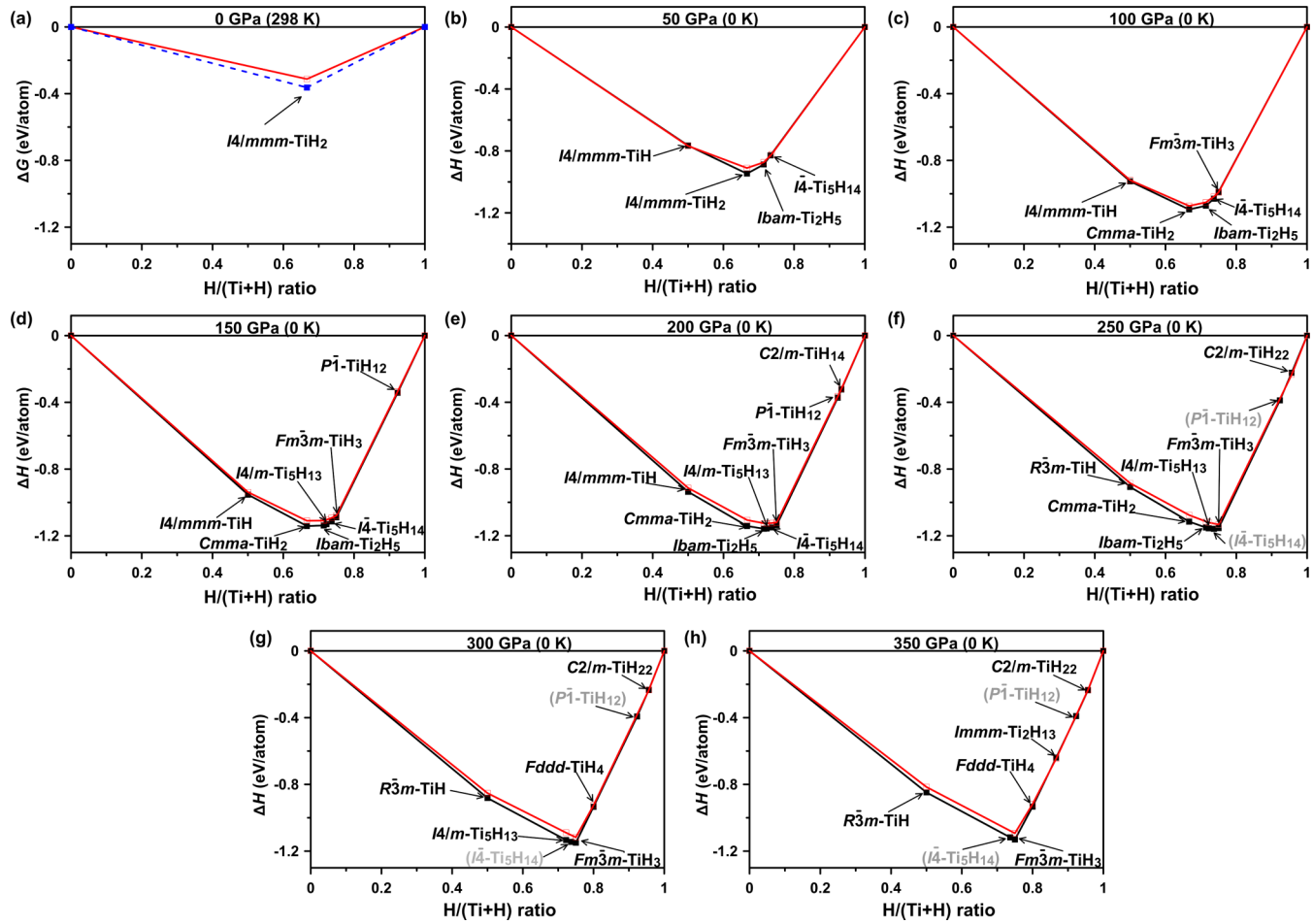

FIG. 1. Convex hull diagrams for the Ti-H system at (a) 0, (b) 50, (c) 100, (d) 150, (e) 200, (f) 250, (g) 300, and (h) 350 GPa. The blue dashed convex hull at 0 GPa shows the experimental result [55]. Black lines with solid squares and red lines with open squares, respectively, represent the calculated results without and with ZPE. The structures indicated in gray are those that lose stability after considering ZPE.

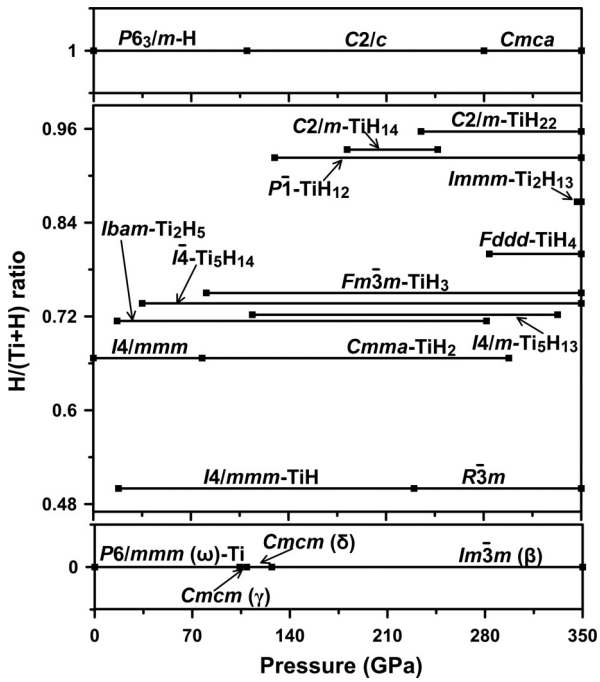

FIG. 2. Pressure-composition phase diagram of the Ti-H system.

phases are shown in Fig. 3, and their structural parameters are listed in Table S1 in the Supplemental Material [38].

For TiH, it should be noted that the enthalpy of $P4_2/mmc$-TiH is lower than that of $I4/mmm$-TiH between 0–8 GPa (see also Fig. 4) which is consistent with the aforementioned calculation [56]. However, $P4_2/mmc$-TiH is not thermodynamically stable from 0 to 8 GPa. With pressure increasing to 18 GPa, TiH ($I4/mmm$) begins to become stable and transforms into $R\bar{3}m$-TiH at 230 GPa. In addition, our calculations reveal a tetragonal ($I4/mmm$) to orthorhombic ($Cmma$) phase transition in TiH_2 at 78 GPa. The high-pressure $Cmma$-TiH_2 persists up to 298 GPa, above which TiH_2 is unstable. Note that the enthalpy difference between $Cmma$-TiH_2 and $P4/nmm$-TiH_2 is very small, due to the similarity of these structures.

The structure of $Fm\bar{3}m$-TiH_3 has an fcc sublattice of Ti atoms, all octahedral and tetrahedral voids of which are occupied by H atoms. It appears at 81 GPa, and continues to be stable up to at least 350 GPa. $Immm$-TiH_6, which was reported to be stable above 175 GPa [56], is actually a metastable phase and decomposes into $Fm\bar{3}m$-TiH_3 and $P\bar{1}$-TiH_{12} at high pressure according to our results. Ti_2H_{13}, a stoichiometry close to TiH_6, emerges on the phase diagram at 347 GPa and adopts a $Immm$ structure. TiH_{14} is stable from 182 to 247 GPa.

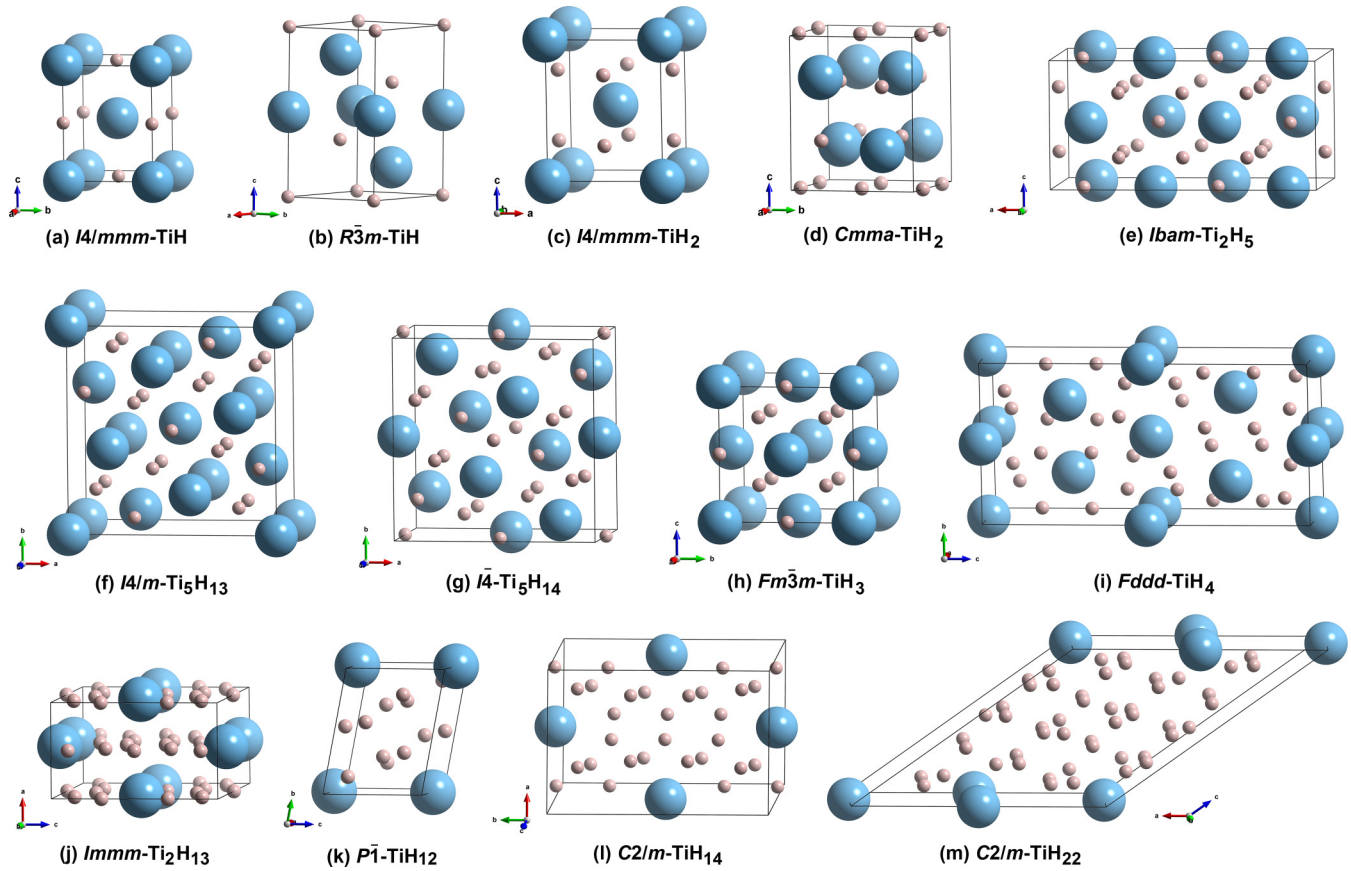

FIG. 3. Crystal structures of titanium hydrides. Large spheres represent titanium atoms and small ones represent hydrogen atoms.

Although both TiH_{14} and SnH_{14} [23] crystallize in $C2/m$ space group, their structures and their hydrogen sublattices are different.

The structure of $Fddd$-TiH_4 consists of titanium atoms which are sandwiched between two slightly distorted H-graphene layers [Fig. 5(b)] in different orientations, forming a $AA_1A_2A_3AA_1A_2A_3A$... stacking sequence [Fig. 5(a)]. The distorted H-graphene layer is drawn in Fig. 5(c); the distance between two layers is 1.373 Å at 350 GPa, as seen in Fig. 5(b). Another interesting finding is that aside from hydrogen-rich TiH_{14} stoichiometry mentioned above, an *extremely* H-rich structure TiH_{22} is identified to be thermodynamically stable at pressures above 235 GPa. To the best of our knowledge, $C2/m$-TiH_{22} is the second hydrogen-richest hydride known or predicted to date, after another transition metal hydride

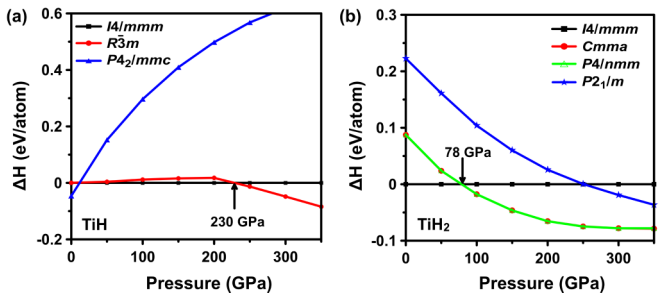

FIG. 4. Enthalpy as a function of pressure (without ZPE) for phases of (a) TiH, referenced to the $I4/mmm$-TiH phase, and (b) TiH_2, referenced to the $I4/mmm$-TiH_2 one.

$C2/c$-YH_{24} [57]. The polyhedral representation of the crystal structure of $C2/m$-TiH_{22} [depicted in Fig. 6(a)] highlights the TiH_{20} polyhedra with Ti-H distances of 1.62–1.66 Å (around each Ti atom, we find 6 H_2 molecules with H-H distance of 0.82 Å, and 8 single hydrogen atoms). Face-sharing TiH_{20} polyhedra form infinite chains running along the b-axis. Between these polyhedral chains, there are boat-type chains of hydrogen atoms with H-H distance of 0.95 Å. This is a very unusual, but aesthetically pleasing and scienitifically interesting crystal structure with 1D monatomic hydrogen chains and coordination polyhedra containing H_2 molecules. The band structure and density of states (DOS) of $C2/m$-TiH_{22} at 350 GPa [Fig. 6(d)] indicate metallicity of TiH_{22}. The total DOS of $C2/m$-TiH_{22} near the Fermi level $N(\varepsilon_F)$ mostly comes from H atoms, which is opposite to $Fddd$-TiH_4 [Fig. 5(d)]. The coexistence of molecular hydrogen with an H-H distance of 0.819 Å and hydrogen chain is clearly revealed by the electron localization function (ELF). As shown in ELF [Fig. 6(c)], the regions with ELF values of 0.7 include H_2 molecules and hydrogen chains, which indicates significant covalent bonding between hydrogen atoms.

In our phonon calculations at high pressure (displayed in Figs. 7 and S1), no imaginary vibrational frequencies are found in the whole Brillouin zone, indicating the dynamical stability of all the predicted structures. Phonon dispersion curves, phonon density of states, phonon linewidths $\gamma_{\mathbf{q}\nu}$, Eliashberg phonon spectral function $\alpha^2F(\omega)$, and the electron-phonon coupling parameter λ of $Immm$-Ti_2H_{13}, $C2/m$-TiH_{22}, $I\bar{4}$-Ti_5H_{14}, $P\bar{1}$-TiH_{12}, $R\bar{3}m$-TiH,

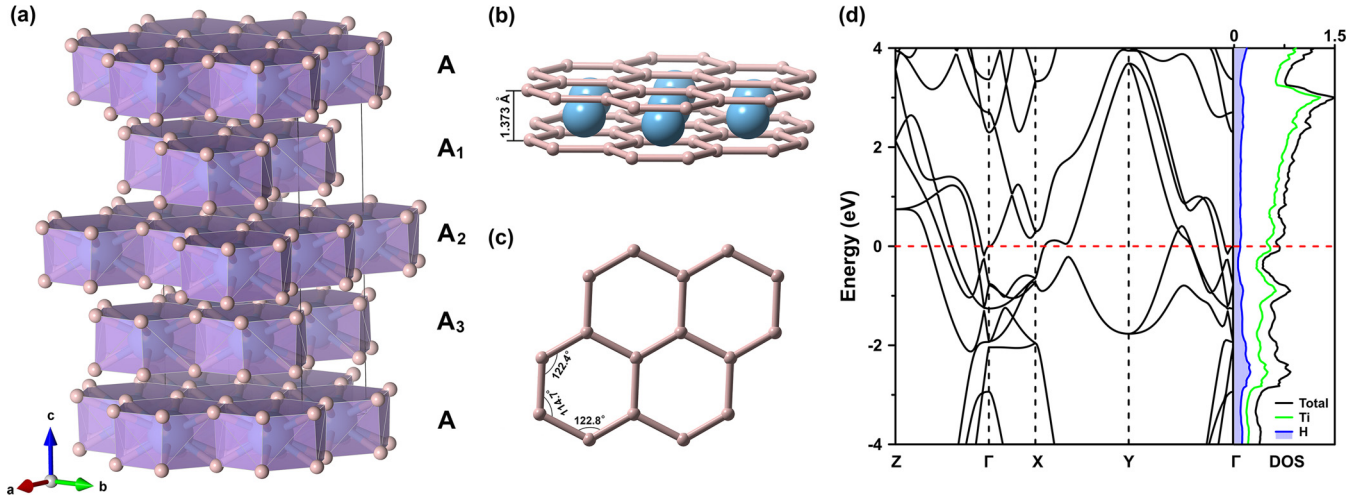

FIG. 5. (a) Polyhedral representation of the $Fddd$-TiH_4 structure. Ti-centered hexagonal prisms are shown in purple. (b) The fundamental "sandwich" of TiH_4. (c) Distorted H-graphene layer in $Fddd$-TiH_4, and (d) electronic band structure and density of states (DOS) of $Fddd$-TiH_4 at 300 GPa; DOS is in the unit of states/eV/formula and Fermi energy (red dashed line) is set to zero.

and $Fddd$-TiH_4, at selected pressures are depicted in Fig. 7. As expected (due to atomic masses), low-frequency modes are mostly related to Ti atoms whereas high-frequency modes are dominated by vibrations of H ones. Moreover, in all of these six structures, the $\gamma_{\mathbf{q}\nu}$ of branches near the Γ point are much greater than those elsewhere in the Brillouin zone. The total λ of $R\bar{3}m$-TiH is mainly contributed by the acoustic modes, whereas those of the other five structures are dominated by optical branches.

We further probe superconductivity of these hydrides, using BCS theory. The calculated superconducting properties are summarized in Table I. All of the predicted titanium hydrides exhibit superconductivity at high pressures. The highest T_c of titanium hydrides are possessed by $Immm$-Ti_2H_{13}, $C2/m$-TiH_{22}, $I\bar{4}$-Ti_5H_{14}, $P\bar{1}$-TiH_{12}, $R\bar{3}m$-TiH, and $Fddd$-TiH_4. $I4/mmm$-TiH_2 exhibits low T_c values (3 mK, $\mu^* = 0.1$) at 50 GPa. Superconductivity of titanium monohydride (TiH) comes largely from strong coupling of the electrons with Ti vibrations, and coupling with H vibrations becomes more important as H content increases. Intriguingly, it is $Immm$-Ti_2H_{13} instead of $C2/m$-TiH_{22} that possesses the highest T_c among searched titanium hydrides. The results from the previous studies [5,25] suggest higher hydrogen content in the binary hydrides is one of the necessary prerequisites to obtain higher T_c value. This is not necessarily always the case; the hydrogen content in $C2/m$-TiH_{22} is much higher than in $Immm$-Ti_2H_{13}. Indeed, $\omega_{\log}$ of $C2/m$-TiH_{22} is larger than that of $Immm$-Ti_2H_{13}. However, this is offset by the lower λ of $C2/m$-TiH_{22} ($\lambda = 0.861$) compared with that of $Immm$-Ti_2H_{13} ($\lambda = 1.423$). The $\alpha^2F(\omega)$ was used for

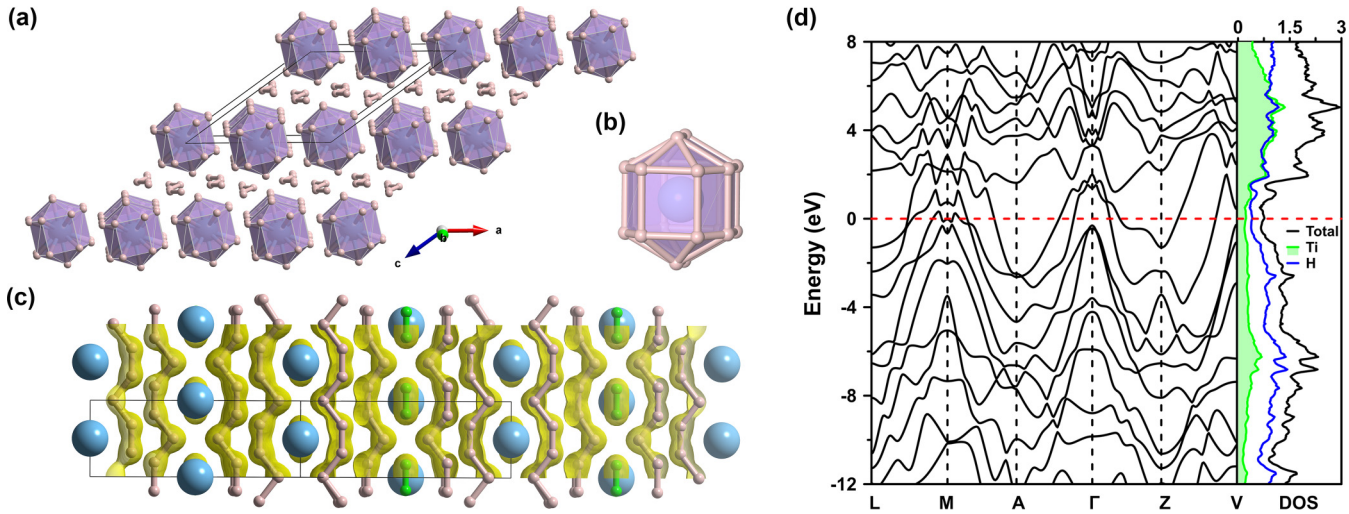

FIG. 6. (a) Polyhedral representation of the $C2/m$-TiH_{22} structure. (b) Expanded view of a H_{20} cage encapsulating a Ti atom. (c) ELF isosurface (ELF = 0.7) for $C2/m$-TiH_{22} at 350 GPa. Green and pink atoms represent molecular hydrogen and hydrogen chains, respectively. (d) Electronic band structure and DOS for $C2/m$-TiH_{22} at 350 GPa; DOS is in the unit of states/eV/formula and Fermi energy (red dashed line) is set to zero.

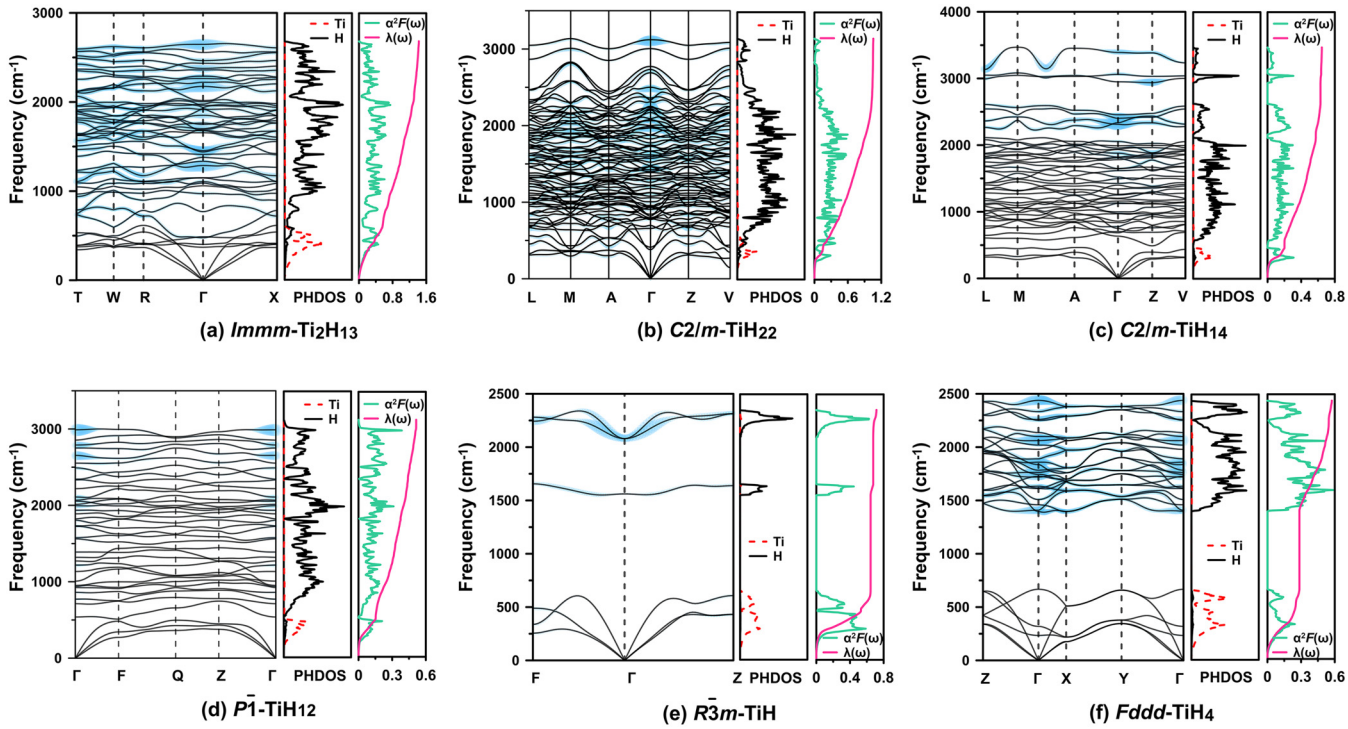

FIG. 7. Phonon dispersion curves, atom-projected phonon density of states, Eliashberg spectral function $\alpha^2F(\omega)$, and the electron-phonon coupling (EPC) parameter λ for (a) $Immm$-Ti_2H_{13} at 350 GPa, (b) $C2/m$-TiH_{22} at 250 GPa, (c) $C2/m$-TiH_{14} at 200 GPa, (d) $P\bar{1}$-TiH_{12} at 350 GPa, (e) $R\bar{3}m$-TiH at 200 GPa, and (f) $Fddd$-TiH_4 at 350 GPa. The magnitude of the phonon linewidths is indicated by the size of the blue haze, which is proportional to the respective coupling strength.

numerically solving the Eliashberg equations and the obtained T_c of $Immm$-Ti_2H_{13} is in the range 110.4–131.2 K ($\lambda = 1.423$, $\mu^* = 0.1$–0.15) at 350 GPa.

For $Immm$-Ti_2H_{13} at 350 GPa and $C2/m$-TiH_{22} at 250 GPa, the dependence of the maximum value of the order parameter on temperature for selected μ^* is presented in Figs. 8(c) and

TABLE I. The EPC parameter λ, electronic density of states at Fermi level $N(\varepsilon_F)$ (states/spin/Ry/formula), the logarithmic average phonon frequency $\omega_{\log}$ (K), and superconducting critical temperatures T_c (K) for titanium hydrides at different pressure P (GPa). T_c values are given for $\mu^* = 0.1$ and T_c in brackets are for $\mu = 0.15$; T_c (McM) is the numerical solution of solving the imaginary-axis Eliashberg equation, T_c (A–D) is calculated from the Allen-Dynes formula, and T_c (E) is obtained by Allen-Dynes modified McMillan formula.

Compound	P	λ	$N(\varepsilon_F)$	$\omega_{\log}$	T_c (E)	T_c (A–D)	T_c (McM)
$C2/m$-TiH_{22}	350	0.861	4.765	1677.4	90.7 (65.0)	93.6 (67.3)	100.0 (78.4)
	250	1.057	4.867	1296.2	98.1 (76.7)	103.1 (80.7)	110.2 (91.3)
$C2/m$-TiH_{14}	200	0.645	5.243	1201.7	33.9 (19.7)	35.0 (20.3)	35.9 (25.0)
$P\bar{1}$-TiH_{12}	350	0.514	3.213	1357.6	18.4 (7.8)	18.8 (8.0)	19.5 (11.5)
	150	0.403	3.748	1074.8	4.7 (1.0)	4.8 (1.0)	5.4 (2.4)
$Immm$-Ti_2H_{13}	350	1.423	10.028	1101.3	119.3 (100.8)	131.2 (110.4)	149.4 (127.4)
$Fddd$-TiH_4	350	0.574	3.803	1034.4	20.6 (10.4)	21.2 (10.7)	20.1 (6.2)
$Fm\bar{3}m$-TiH_3	100	0.528	6.798	459.4	6.9 (3.1)	7.1 (3.1)	7.5 (4.7)
$I\bar{4}$-Ti_5H_{14}	350	0.411	20.738	479.9	2.4 (0.6)	2.4 (0.6)	2.8 (1.4)
	50	0.477	35.785	525.6	5.3 (1.9)	5.4 (2.0)	5.8 (3.3)
$I4/m$-Ti_5H_{13}	300	0.470	22.211	412.6	3.9 (1.4)	4.0 (1.4)	4.4 (2.7)
	150	0.406	27.253	450.8	2.1 (0.5)	2.1 (0.5)	2.5 (1.1)
$Ibam$-Ti_2H_5	250	0.504	9.910	363.3	4.6 (1.9)	4.7 (1.9)	5.1 (3.2)
	50	0.564	12.852	365.0	6.9 (3.4)	7.1 (3.5)	6.9 (4.6)
$Cmma$-TiH_2	250	0.509	3.604	434.3	5.7 (2.4)	5.8 (2.4)	6.0 (3.7)
$I4/mmm$-TiH_2	50	0.227	3.687	349.4	0.0 (0.0)	0.0 (0.0)	0.0 (0.0)
$R\bar{3}m$-TiH	350	0.714	4.328	597.3	21.8 (13.9)	22.7 (14.4)	23.9 (18.2)
$I4/mmm$-TiH	200	0.991	6.303	264.3	18.1 (13.8)	19.5 (14.8)	22.5 (18.9)
	50	1.013	8.716	71.0	5.0 (3.9)	5.4 (4.1)	12.6 (10.0)

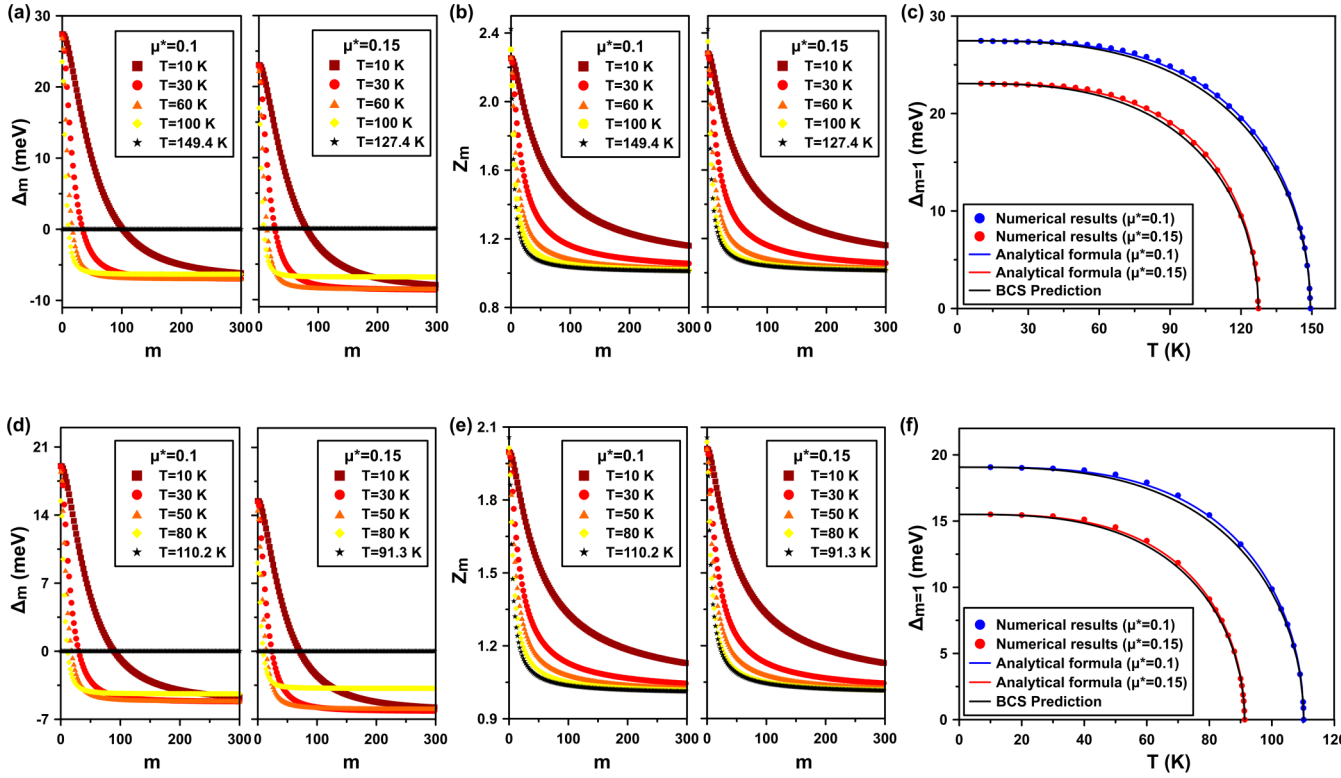

FIG. 8. Dependence of the superconducting order parameter on the number m for select values of temperature and Coulomb pseudopotential for (a) $Immm$-Ti_2H_{13} at 350 GPa and (d) $C2/m$-TiH_{22} at 250 GPa. The wave-function renormalization factor Z_m on the imaginary axis for select values of temperature and Coulomb pseudopotential for (b) $Immm$-Ti_2H_{13} and (e) $C2/m$-TiH_{22}. The influence of temperature on the maximum value of the order parameter ($\Delta_{m=1}$) for selected μ^* of (c) $Immm$-Ti_2H_{13} and (f) $C2/m$-TiH_{22}. Solid circles correspond to the exact numerical solutions of the Eliashberg equations, the red and blue lines represent the results obtained using analytical formula [Eq. (10)]. Black lines are predicted by BCS model [Eq. (10), where $\Gamma = 3$].

8(f). The maximum value of order parameter $\Delta_{m=1}$ decreases with the growth of T and μ^*. On the basis of these results, the $\Delta_{m=1}$ value can be characterized analytically by means of the phenomenological formula

$$\Delta_{m=1}(T, \mu^*) = \Delta_{m=1}(T_0, \mu^*)\sqrt{1 - \left(\frac{T}{T_c}\right)^{\Gamma}}. \qquad (10)$$

For the maximum value of order parameter $\Delta_{m=1}$, we obtained the estimation of temperature exponent for $Immm$-Ti_2H_{13} ($\Gamma = 3.25$ for $\mu^* = 0.1$; $\Gamma = 3.31$ for $\mu^* = 0.15$) at 250 GPa and $C2/m$-TiH_{22} ($\Gamma = 3.21$ for $\mu^* = 0.1$; $\Gamma = 3.16$ for $\mu^* = 0.15$) at 250 GPa. It is clear that the temperature dependence of maximum order parameter obtained in Eliashberg equations only differs a little bit from the results estimated by the BCS theory, where $\Gamma = 3$ (Ref. [58]). The increase of the Coulomb pseudopotential μ^* leads to a strong decrease of the order parameter [Figs. 8(a) and 8(d)], with only small perturbations to the wave-function renormalization factor [Figs. 8(b) and 8(e)]. This indicates that the influence of the depairing interaction between the electrons is more significant on the energy required to break a Cooper pair (Cooper pairs need to be "broken apart" by giving to the system an energy equal to 2Δ where Δ is the energy gap [59]) than on the enhancement of the electron mass arising from the electron-phonon interaction.

Through comparison among above three approaches of calculating T_c, it can be seen that the Allen-Dynes formula much better reproduces the numerical results than the modified McMillan one. Specifically, two analytical equations are satisfactory when λ is small (< 0.8), while the underestimation of analytical approaches become obvious when λ is large (> 0.8). This is well within expectations that these two analytical formulas can give accurate T_c values for weak-coupling superconductors, while they become less satisfactory as the coupling increases. The limitation of these two analytic formulas is inherently due to the fact that they are empirical formulas derived from the numerical solution of the Eliashberg equation of three spectra, namely, Pb, Hg, and Einstein spectra; when $\alpha^2F(\omega)$ deviates greatly from these three spectra, the accuracy of the analytic formulas decreases [60].

The influence of pressure on T_c has been widely discussed before. Theoretical studies of some systems [5,61,62] show the decrease of T_c will decrease with increasing pressure; other compounds [63,64] display T_c increasing with pressure; yet others [65,66] reveal negligible pressure dependence. Although the values of T_c listed in Table I are not sufficient to completely determine the impact of pressure on T_c, it still can be seen that pressure has a negative effect on T_c of $C2/m$-TiH_{22}, $I\bar{4}$-Ti_5H_{14}, $Ibam$-Ti_2H_5, and $I4/mmm$-TiH, while it has a positive effect on that of $P\bar{1}$-TiH_{12} and

$I4/m$-Ti_5H_{13}. In all of these compounds pressure evolution of T_c mostly follows the evolution of lambda.

IV. CONCLUSIONS

In order to discover high-T_c superconductors, the Ti-H system at pressures up to 350 GPa was systematically explored using the *ab initio* evolutionary algorithm USPEX. A new phase of TiH ($R\bar{3}m$-TiH) and several stable compounds with new stoichiometries ($C2/m$-TiH_{22}, $P\bar{1}$-TiH_{12}, $Immm$-Ti_2H_{13}, $Fddd$-TiH_4, $I\bar{4}$-Ti_5H_{14}, $I4/m$-Ti_5H_{13}, and $Ibam$-Ti_2H_5) were predicted, and found to be dynamically stable in their predicted pressure ranges of stability. With increasing pressure, $I4/mmm$-TiH transforms into $R\bar{3}m$-TiH at 230 GPa, and $I4/mmm$-TiH_2 into $Cmma$-TiH_2 at 78 GPa. $Cmma$-TiH_2 is structurally similar to $P4/nmm$-TiH_2. $C2/m$-TiH_{22} has the highest hydrogen content among all titanium hydrides, and contains TiH_{20} cages. The estimated T_c of $Immm$-Ti_2H_{13} is 127.4–149.4 K ($\mu^* = 0.1$–0.15) at 350 GPa, which is actually higher than T_c of the aforementioned $C2/m$-TiH_{22} of 91.3–110.2 K ($\mu^* = 0.1$–0.15) at 250 GPa. Superconductivity of $Immm$-Ti_2H_{13} mainly arises from both strong coupling of the electrons with H vibrations and the large logarithmic average phonon frequency. The accuracy of three methods for estimating the T_c was compared. Taking solution of the Eliashberg equations as standard, the estimated T_c from Allen-Dynes formula is more accurate than that from the modified McMillan expression. The constructed pressure-composition phase diagram and the analysis of superconductivity of titanium hydrides will motivate future experimental synthesis of titanium hydrides and studies of their high-temperature superconductivity.

ACKNOWLEDGMENTS

J.M.M. acknowledges startup support from Washington State University and the Department of Physics and Astronomy thereat. A.R.O. thanks Russian Science Foundation (Grant No. 19-72-30043) for financial support. Calculations were performed on the QSH supercomputer at Stony Brook University and institutional cluster (IC) provided by the Scientific Data and Computing Center (SDCC) at Brookhaven National Laboratory (BNL).

[1] V. L. Ginzburg, Phys.-Usp. **42**, 353 (1999).
[2] D. Van Delft and P. Kes, Phys. Today **63**(9), 38 (2010).
[3] D. Duan, Y. Liu, F. Tian, D. Li, X. Huang, Z. Zhao, H. Yu, B. Liu, W. Tian, and T. Cui, Sci. Rep. **4**, 6968 (2014).
[4] A. Drozdov, M. Eremets, I. Troyan, V. Ksenofontov, and S. Shylin, Nature (London) **525**, 73 (2015).
[5] H. Liu, I. I. Naumov, R. Hoffmann, N. Ashcroft, and R. J. Hemley, Proc. Natl. Acad. Sci. U. S. A. **114**, 6990 (2017).
[6] T. Bi, N. Zarifi, T. Terpstra, and E. Zurek, *Reference Module in Chemistry, Molecular Sciences and Chemical Engineering* (Elsevier, 2019).
[7] M. Somayazulu, M. Ahart, A. K. Mishra, Z. M. Geballe, M. Baldini, Y. Meng, V. V. Struzhkin, and R. J. Hemley, Phys. Rev. Lett. **122**, 027001 (2019).
[8] A. Drozdov, P. Kong, V. Minkov, S. Besedin, M. Kuzovnikov, S. Mozaffari, L. Balicas, F. Balakirev, D. Graf, V. Prakapenka *et al.*, Nature (London) **569**, 528 (2019).
[9] B. Lorenz and C. Chu, *Frontiers in Superconducting Materials* (Springer, Berlin, 2005), pp. 459–497.
[10] L. Gao, Y. Y. Xue, F. Chen, Q. Xiong, R. L. Meng, D. Ramirez, C. W. Chu, J. H. Eggert, and H. K. Mao, Phys. Rev. B **50**, 4260 (1994).
[11] N. W. Ashcroft, Phys. Rev. Lett. **21**, 1748 (1968).
[12] N. W. Ashcroft, Phys. Rev. Lett. **92**, 187002 (2004).
[13] N. W. Ashcroft, J. Phys.: Condens. Matter **16**, S945 (2004).
[14] Y. Xie, Q. Li, A. R. Oganov, and H. Wang, Acta Crystallogr. C **70**, 104 (2014).
[15] X. Feng, J. Zhang, G. Gao, H. Liu, and H. Wang, RSC Adv. **5**, 59292 (2015).
[16] H. Wang, S. T. John, K. Tanaka, T. Iitaka, and Y. Ma, Proc. Natl. Acad. Sci. U. S. A. **109**, 6463 (2012).
[17] X. Ye, N. Zarifi, E. Zurek, R. Hoffmann, and N. Ashcroft, J. Phys. Chem. C **122**, 6298 (2018).
[18] X.-F. Li, Z.-Y. Hu, and B. Huang, Phys. Chem. Chem. Phys. **19**, 3538 (2017).
[19] Y. Liu, X. Huang, D. Duan, F. Tian, H. Liu, D. Li, Z. Zhao, X. Sha, H. Yu, H. Zhang *et al.*, Sci. Rep. **5**, 11381 (2015).
[20] Q. Zhuang, X. Jin, T. Cui, Y. Ma, Q. Lv, Y. Li, H. Zhang, X. Meng, and K. Bao, Inorg. Chem. **56**, 3901 (2017).
[21] K. Abe and N. W. Ashcroft, Phys. Rev. B **88**, 174110 (2013).
[22] I. A. Kruglov, D. V. Semenok, H. Song,, I. A. Wrona, R. Akashi, M. Esfahani, D. Duan, T. Cui, A. G. Kvashnin, and A. R. Oganov, Phys. Rev. B **101**, 024508 (2020).
[23] M. M. D. Esfahani, Z. Wang, A. R. Oganov, H. Dong, Q. Zhu, S. Wang, M. S. Rakitin, and X.-F. Zhou, Sci. Rep. **6**, 22873 (2016).
[24] J. A. Flores-Livas, A. Sanna, and E. Gross, Eur. Phys. J. B **89**, 63 (2016).
[25] X. Zhong, H. Wang, J. Zhang, H. Liu, S. Zhang, H.-F. Song, G. Yang, L. Zhang, and Y. Ma, Phys. Rev. Lett. **116**, 057002 (2016).
[26] D. V. Semenok, I. A. Kruglov, I. A. Savkin, A. G. Kvashnin, and A. R. Oganov, arXiv:1806.00865 [Curr. Opin. in Solid State & Mater. Sci. (to be published).
[27] H. Yakel, Acta Crystallogr. **11**, 46 (1958).
[28] A. San-Martin and F. Manchester, Bull. Alloy Phase Diagr. **8**, 30 (1987).
[29] R. S. Vennila, A. Durygin, M. Merlini, Z. Wang, and S. Saxena, Int. J. Hydrog. Energy **33**, 6667 (2008).
[30] P. E. Kalita, S. V. Sinogeikin, K. Lipinska-Kalita, T. Hartmann, X. Ke, C. Chen, and A. Cornelius, J. Appl. Phys. **108**, 043511 (2010).
[31] N. Endo, H. Saitoh, A. Machida, Y. Katayama, and K. Aoki, J. Alloys Compd. **546**, 270 (2013).
[32] K. V. Shanavas, L. Lindsay, and D. S. Parker, Sci. Rep. **6**, 28102 (2016).
[33] A. R. Oganov and C. W. Glass, J. Chem. Phys. **124**, 244704 (2006).

[34] A. R. Oganov, A. O. Lyakhov, and M. Valle, Acc. Chem. Res. **44**, 227 (2011).

[35] A. O. Lyakhov, A. R. Oganov, H. T. Stokes, and Q. Zhu, Comput. Phys. Commun. **184**, 1172 (2013).

[36] J. P. Perdew, K. Burke, and M. Ernzerhof, Phys. Rev. Lett. **77**, 3865 (1996).

[37] G. Kresse and J. Furthmüller, Phys. Rev. B **54**, 11169 (1996).

[38] See Supplemental Material at http://link.aps.org/supplemental/10.1103/PhysRevB.101.134108 for the composition statistic of crystal structure searching (Fig. S1); phonon dispersion curves, phonon density of states projected onto selected atoms, Eliashberg spectral function $\alpha^2F(\omega)$, and the electron-phonon coupling parameter λ of predicted titanium hydrides at high pressures (Fig. S2) and the calculated structural parameters (Table S1).

[39] P. E. Blöchl, Phys. Rev. B **50**, 17953 (1994).

[40] G. Kresse and D. Joubert, Phys. Rev. B **59**, 1758 (1999).

[41] A. Togo, F. Oba, and I. Tanaka, Phys. Rev. B **78**, 134106 (2008).

[42] S. Baroni, S. De Gironcoli, A. Dal Corso, and P. Giannozzi, Rev. Mod. Phys. **73**, 515 (2001).

[43] P. Giannozzi, S. Baroni, N. Bonini, M. Calandra, R. Car, C. Cavazzoni, D. Ceresoli, G. L. Chiarotti, M. Cococcioni, I. Dabo *et al.*, J. Phys.: Condens. Matter **21**, 395502 (2009).

[44] P. Giannozzi, O. Andreussi, T. Brumme, O. Bunau, M. B. Nardelli, M. Calandra, R. Car, C. Cavazzoni, D. Ceresoli, M. Cococcioni, N. Colonna, I. Carnimeo, A. D. Corso, S. de Gironcoli, P. Delugas, R. A. DiStasio, Jr., A. Ferretti, A. Floris, G. Fratesi, G. Fugallo *et al.*, J. Phys.: Condens. Matter **29**, 465901 (2017).

[45] C. Grimaldi, L. Pietronero, and M. Scattoni, Eur. Phys. J. B **10**, 247 (1999).

[46] A. B. Migdal, Sov. Phys.–JETP **7**, 996 (1958).

[47] J. Carbotte, Rev. Mod. Phys. **62**, 1027 (1990).

[48] P. B. Allen and B. Mitrović, *Solid State Physics* (Elsevier, 1983), Vol. 37, pp. 1–92.

[49] R. Szczęśniak, Acta Phys. Pol. A **109**, 179 (2006).

[50] R. Szczęśniak, D. Szczęśniak, and E. Drzazga, Solid State Commun. **152**, 2023 (2012).

[51] W. McMillan, Phys. Rev. **167**, 331 (1968).

[52] R. Dynes, Solid State Commun. **10**, 615 (1972).

[53] P. B. Allen and R. Dynes, Phys. Rev. B **12**, 905 (1975).

[54] K. T. Chan, B. D. Malone, and M. L. Cohen, Phys. Rev. B **86**, 094515 (2012).

[55] M. W. Chase, *NIST-JANAF Thermochemical Tables 2 Volume-Set (Journal of Physical and Chemical Reference Data Monographs)*, Vol. 2 (Wiley New York, 1998).

[56] Q. Zhuang, X. Jin, T. Cui, D. Zhang, Y. Li, X. Li, K. Bao, and B. Liu, Phys. Rev. B **98**, 024514 (2018).

[57] F. Peng, Y. Sun, C. J. Pickard, R. J. Needs, Q. Wu, and Y. Ma, Phys. Rev. Lett. **119**, 107001 (2017).

[58] G. Varelogiannis, Z. Phys. B: Condens. Matter **104**, 411 (1997).

[59] M. Tortello and D. Daghero, in *Superconductors*, edited by A. Gabovich (IntechOpen, Rijeka, 2015), Chap. 8.

[60] J.-D. Cai, G.-D. Ji, H.-S. Wu, J.-H. Cai, and C.-D. Gong, Acta Phys. Sin. **28**, 393 (1979).

[61] S. Yu, X. Jia, G. Frapper, D. Li, A. R. Oganov, Q. Zeng, and L. Zhang, Sci. Rep. **5**, 17764 (2015).

[62] A. G. Kvashnin, D. V. Semenok, I. A. Kruglov, I. A. Wrona, and A. R. Oganov, ACS Appl. Mater. Interfaces **10**, 43809 (2018).

[63] D. Y. Kim, R. H. Scheicher, H.-k. Mao, T. W. Kang, and R. Ahuja, Proc. Natl. Acad. Sci. U. S. A. **107**, 2793 (2010).

[64] Y. Li, J. Hao, H. Liu, Y. Li, and Y. Ma, J. Chem. Phys. **140**, 174712 (2014).

[65] S. Zhang, Y. Wang, J. Zhang, H. Liu, X. Zhong, H.-F. Song, G. Yang, L. Zhang, and Y. Ma, Sci. Rep. **5**, 15433 (2015).

[66] S. Zheng, S. Zhang, Y. Sun, J. Zhang, J. Lin, G. Yang, and A. Bergara, Front. Phys. **6**, 101 (2018).